Earth Planet. Sci. Lett. 673 (2026) 119720

Contents lists available at ScienceDirect

Earth and Planetary Science Letters

journal homepage: www.elsevier.com/locate/epsl

The lithosphere - asthenosphere system seen by surface waves: New insights from radial anisotropy

S. Durand*, E. Debayle, Y. Ricard

Universite Claude Bernard Lyon 1, ENS de Lyon, CNRS, UMR 5276 LGL-TPE, France

ARTICLE INFO

Editor: H. Thybo

Keywords:
Radial anisotropy
Lithosphere - asthenosphere system
Tomography
Surface waves

ABSTRACT

We propose a conceptual model of the lithosphere-asthenosphere system that reconciles a number of surface wave observations. It comes in the context of the development of a new SV wave velocity, V_{sv}, and radial anisotropy, ξ, global model based on multi-mode Rayleigh and Love wave data. The Rayleigh dataset has also been used in previous studies to constrain the azimuthal anisotropy, the quality factor Q and the melt content. All these models are based on self-consistent datasets and use the same waveform modeling and tomographic approaches, with similar regularization and smoothing. The first important finding of this study is the fact that a 1-D ξ model close to PREM but including a 3D crust structure explains our dataset almost everywhere, except in oldest parts of the continents (mainly Archean and Proterozoic terrains) and youngest parts of the Pacific ridge (mainly ages ≤ 50 Ma) where 3-D variations of ξ are required. Based on this, we build an hybrid model, Hybrid 1D/3D, where ξ is fixed to a 1-D profile when sufficient to fit the data, and inverted for when the dataset requires lateral variations. Our radially anisotropic model shows that there is no age dependance of the radial anisotropy ξ in the oceanic lithosphere while age is the main parameter controlling V_{sv}, melt content and azimuthal anisotropy, particularly under fast plates. We also find that positive radial anisotropy ($\xi > 1$) extends deeper beneath oceans (down to 350 km depth) than beneath continents. We propose that the thicker radially anisotropic layer under the oceans compared to the continent indicates a change in origin from frozen-only anisotropy under the continent to a more complex situation under the oceans. Cratons appear fast, melt-free and anisotropic, down to 200-250 km depth, and anomalies with $\xi \leq 1$ are present in the deeper part of the cratonic roots (around 250 km) that could reflect past delamination or compression of the deep lithospheric roots.

1. Introduction

The transition from the conducting stiff lithosphere to the weaker convecting asthenosphere is referred to as the lithosphere - asthenosphere boundary (LAB) and the ensemble including their interaction is the lithosphere - asthenosphere system. The LAB marks a rheological transition that plays a key role in tectonics but its origin is still debated. Seismic studies have provided many observations of a velocity minimum that makes the transition from the seismically fast upper layer, interpreted as the lithosphere, and the deeper and slower region, interpreted as the asthenosphere. This transition is clearly observed under oceans from different kind of seismic data (e.g. Nishimura and Forsyth, 1989; Zhang and Tanimoto, 1991; Debayle and Ricard, 2012; Priestley and McKenzie, 2013; Auer et al., 2015; Audhkhasi and Singh, 2022), while seismic observations are more difficult to reconcile under cratons (e.g. Rychert et al., 2010; Hua et al., 2023; Boyce et al., 2024). Other properties besides seismic velocities have also been investigated such as seismic anisotropy (e.g. Montagner and Tanimoto, 1991; Debayle and Ricard, 2013; Burgos et al., 2014; Beghein et al., 2014; Hua et al., 2025) and attenuation (e.g. Billien et al., 2000; Dalton et al., 2008; Gung and Romanowicz, 2004; Ma et al., 2015; Adenis et al., 2017) which all together help to better understand the lithosphere - asthenosphere system. However these properties originate from different studies and different datasets, making it difficult to develop a general understanding. In that context we propose revisiting our understanding of the lithosphere - asthenosphere system using surface waves by combining velocity, anisotropy and attenuation to build a conceptual model.

Surface waves are commonly used to determine shear wave velocities, radial and azimuthal anisotropy, and shear attenuation in the upper mantle (e.g. Nataf et al., 1986; Montagner and Tanimoto, 1991; Trampert and Woodhouse, 1995; Selby and Woodhouse, 2002; Gung et al., 2003; Zhou et al., 2006; Lebedev and Van Der Hilst, 2008; Dalton et al.,

---

* Corresponding author.
E-mail address: stephanie.durand@ens-lyon.fr (S. Durand).

https://doi.org/10.1016/j.epsl.2025.119720
Received 19 June 2025; Received in revised form 25 October 2025; Accepted 6 November 2025

2008; Debayle and Ricard, 2012; Schaeffer and Lebedev, 2013; Burgos et al., 2014; Adenis et al., 2017; Karaoğlu and Romanowicz, 2018; Debayle et al., 2020). They offer very good geographical coverage and, by combining fundamental and higher modes, they provide resolution of their depth variations down to the transition zone (e.g. Ritsema et al., 2004; Schaeffer and Lebedev, 2013; Durand et al., 2015).

Shear velocity, V_s, is the parameter best constrained by surface waves. Recent global V_s models are consistent up to degree 60 in the uppermost 200 km and degree 15 in the transition zone (Chang et al., 2015; Debayle et al., 2016; Priestley et al., 2020; French and Romanowicz, 2014; Simmons et al., 2021; Kustowski et al., 2008). On top of velocities, mapping anisotropy is important as it can be interpreted as a proxy for the mantle flow (e.g. Tanimoto and Anderson, 1984; Silver and Chan, 1991; Montagner, 1994; Savage, 1999; Becker, 2008; Long and Becker, 2010; Auer et al., 2015; Becker and Lebedev, 2021). Azimuthal anisotropy provides information on the horizontal motions, and radial anisotropy on the ratio of horizontal to vertical motions ($\xi = (V_{sh}/V_{sv})^2$ where V_{sh} and V_{sv} are the velocities of horizontally and vertically polarized shear waves (see e.g. Takeuchi and Saito, 1972)). In the presence of a dominant horizontal flow (e.g., in the shallow layers) $\xi > 1$ can be expected. On the contrary, vertical flows should be associated with $\xi < 1$. A complexity of this rule of thumb lies in the fact that the flow that induces the anisotropy may be ongoing or frozen within the lithosphere fabric. While there is a good agreement between the models of azimuthal anisotropy (see e.g. Debayle and Ricard, 2013), existing models of radial anisotropy are less consistent and differ significantly from each other (Ferreira et al., 2010; Chang et al., 2014).

The variable consistency between several global V_s and ξ models is illustrated in Fig. 1. While the correlations between all the V_s models are very high at depths of 100 and 200 km (see e.g. Debayle and Ricard, 2012), the correlations between the ξ models are significantly different as shown in Fig. S1. These differences can be attributed to the use of different datasets, some restricted to surface waves (Priestley et al., 2020), while others including body waves (Kustowski et al., 2008; French and Romanowicz, 2014; Chang et al., 2015; Simmons et al., 2021), and to the use of different tomographic methods, ranging from linear to non-linear waveform inversions. Surface waves have also been used to build S-wave attenuation models of the upper mantle. However, these models, limited in number, are restricted to long wavelengths up to degree 12 and they also significantly differ, revealing the difficulty to robustly measure attenuation as well as differences in inversion strategies (Selby and Woodhouse, 2002; Gung and Romanowicz, 2004; Dalton et al., 2008; Adenis et al., 2017).

In this paper, we first complete these previous studies by adding a new global ξ model built with a waveform inversion approach similar to what we used for our anisotropic V_s and Q_s models (Debayle and Kennett, 2000; Debayle and Ricard, 2012; Ho et al., 2016). The automated waveform approach used previously for Rayleigh waves (Debayle and Ricard, 2012), was adapted to Love waves as described in Ho et al. (2016) and Moulik et al. (2021). After regionalization, we obtain a set of Love and Rayleigh phase velocity maps (e.g. Love and Rayleigh velocity maps as a function of the wave period, see Figs. S2 and S3). We then invert these maps simultaneously to obtain new global V_{sv} and ξ models (e.g. the velocity of vertically polarized S waves, and the radial anisotropy as a function of depth, latitude and longitude). We then interpret the global V_{sv} and ξ models in the light of our previous models of azimuthal anisotropy, shear quality factor Q_s and melt content. These models can be combined to produce a global interpretation because they are self-consistent, in the sense that they are obtained from a similar methodology and inversion technique. The new global ξ model adds further constraints and enables us to build a conceptual model of the lithosphere - asthenosphere system that reconciles all seismic observations. In particular adding radial anisotropy, on top of azimuthal anisotropy, helps to distinguish between regions that are currently deformed or those where deformation is frozen in.

2. Datasets and tomographic inversions

2.1. General strategy

The datasets include ≈ 400 000 Rayleigh waveforms described in Debayle and Ricard (2012), and ≈ 100 000 Love waveforms modeled following Ho et al. (2016) and Moulik et al. (2021). For all our models (V_s and Q_s), the inversion procedure for the surface waves follows a roughly similar method adapted to each specific case. For each path, the observed seismogram is represented by a finite sum of pure-mode synthetics computed for a laterally homogeneous medium. The observed seismograms are adjusted for the fundamental and up to the fifth overtone, for a total of 47 periods, by cross-correlation with a synthetics computed in a reference model consisting of the PREM anisotropic model with a crustal model adapted by averaging the 3SMAC seismic crust along the ray (Nataf and Ricard, 1996). The 3SMAC (three-dimensional seismological model a priori constrained) model is consistent with various geophysical data and is therefore a useful a priori model in seismological inversions. The 3SMAC model is also used to compute the excitation source and the scalar seismic moment is also inverted. This processing leads to an ancillary dataset of ≈ 15 millions Rayleigh phase velocities and quality factors and ≈ 4 millions Love phase velocities and quality factors. The same code with the appropriate modes is used for the two types of waves.

The difference in the number of observations between the two datasets, could enable us to use a shorter correlation length for Rayleigh waves in comparison to Love waves (although the improvement in ray coverage is not proportional with the number of observations, since the ray paths tend to sample the same regions more or less consistently). In order to avoid any potential bias in the $\xi = (V_{sh}/V_{sv})^2$ model, we prefer to select the same correlation length for the Rayleigh and Love models. However, we conducted a series of tests involving the selection of a comparable number of paths in the two datasets. The results are not significantly different. They are summarized in Fig. S4 and will be discussed in the next sections.

Figs. S2 and S3 show the ray densities of our Love and Rayleigh datasets, respectively. The scale indicates the number of rays over an area of 4 by 4 degrees. The ray density is about 3 times lower for Love waves than for Rayleigh waves. However, even in the least covered areas of the Love density maps, more than 10 different paths are crossing each 4 by 4 degree zone. For each ray, the phase velocities for the fundamental modes and five overtones are measured. For the fundamental modes, 13 periods are measured from 40 to 200 s. The number of periods decreases for the overtones and only 3 periods are measured for the fifth overtone. Several examples of phase velocity maps obtained after regionalization using a lateral correlation length of 400 km, are shown in Figs. S2 and S3, for different periods and overtones of Rayleigh and Love waves. The inclusion of overtones gives a very good resolution for the entire upper mantle as illustrated by the sensitivity kernels also displayed in Figs. S2 and S3.

2.2. Previous models of azimuthal anisotropy, attenuation and estimates of melt content

Before discussing radial anisotropy, we briefly review how similar observations were used to build our previous azimuthal anisotropy, attenuation and melt content models.

The model for azimuthal V_{sv} anisotropy is taken from Debayle and Ricard (2012). In this paper, the same set of ≈ 15 millions Rayleigh velocity measurements is used. A path averaged depth-dependent model is derived to explain each seismogram. These depth-dependent models are then regionalized to obtain the $V_{sv}(\theta, \phi, r)$ model, using a lateral correlation length of 400 km. The possible dependence of Rayleigh velocity on the azimuth ψ of the ray, in $\cos(2\psi)$ and $\sin(2\psi)$, is taken into account in the regionalization.

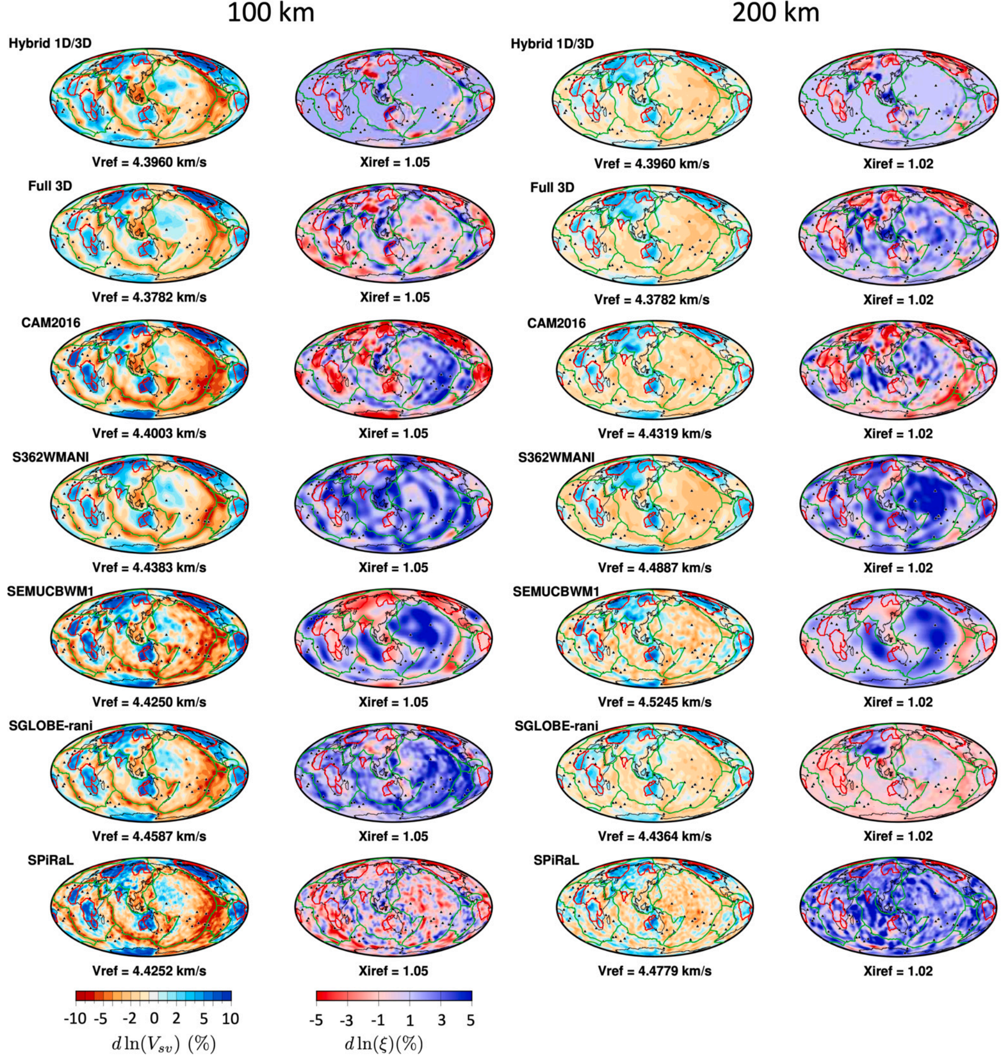

Fig. 1. Comparison of radially anisotropic models. V_{sv} and ξ at 100 and 200 km depth for different tomographic models given in perturbations in % relative to the average value at each depth for V_{sv} (Vref indicated below the maps) and relative to fix reference values at each depth for ξ (Xiref indicated below the maps). The top two rows (Hybrid 1D/3D, Full 3D) are the results from this study. CAM2016: Priestley et al. (2020), S362WMANI: Kustowski et al. (2008), SEMUCB-WM1: French and Romanowicz (2014), SGLOBE-rani: Chang et al. (2015), SPiRaL: Simmons et al. (2021). While V_{sv} models are very consistent in terms of patterns, there is significant disagreement between the different ξ models (see also Fig. S1).

The model for attenuation is taken from Adenis et al. (2017) and again, first involves constructing attenuation maps at different periods and for different overtones. Measuring attenuation is much more difficult than measuring arrival times or velocities and a significant preprocessing must be carried out. Adenis et al. (2017) only retained those measurements for which the inverted scalar seismic moment matched with estimated moment. They removed all rays too close to a source radiation node and corrected the measurement from focusing-defocussing effects (Woodhouse and Wong, 1986). These measurements have been regionalized, inverting for $\ln(Q)$ instead of Q, with a non-linear least-squares method, and using a correlation length, 1000 km, longer than for the other regionalizations. Finally, at each latitude and longitude, a depth-dependent attenuation model was produced.

The model for melt proportion is taken from Debayle et al. (2020). Debayle et al. (2020) compare the model of attenuation with a model of V_{sv} tomography derived as described above, but built with the larger correlation length 1000 km of the attenuation model. The couple velocity/attenuation is then interpreted in the light of experimental velocity/attenuation data as a function of temperature, pressure and melt content (Takei, 2017) from which a melt content is predicted.

All this information is summarized in Table S1. For more details about each model, we refer the reader to each specific studies (Debayle and Ricard (2012) for azimuthal velocities, Adenis et al. (2017) for Q_s and Debayle et al. (2020) for estimations of melt content).

2.3. *Radial anisotropy*

To obtain a model of radial anisotropy, for each period and overtone of our datasets, a phase velocity map is constructed by combining the path averaged phase velocities in a tomographic inversion using a continuous regionalization scheme (Tarantola and Valette, 1982; Debayle and Sambridge, 2004) (see Figs. S2 and S3). The Love and Rayleigh regionalizations are performed with the same regularization parameters, and particularly with the same resolution length of 400 km. For this inversion of radial anisotropy, the azimuthal anisotropic dependence of the Rayleigh and Love waves is neglected due to our excellent azimuthal coverage. The horizontal correlation length must be sufficient to average out the azimutal variations of Love and Rayleigh waves (Debayle and Kennett, 2000). This is a common assumption made in other tomographic inversions that include radial anisotropy (Ferreira et al., 2010;

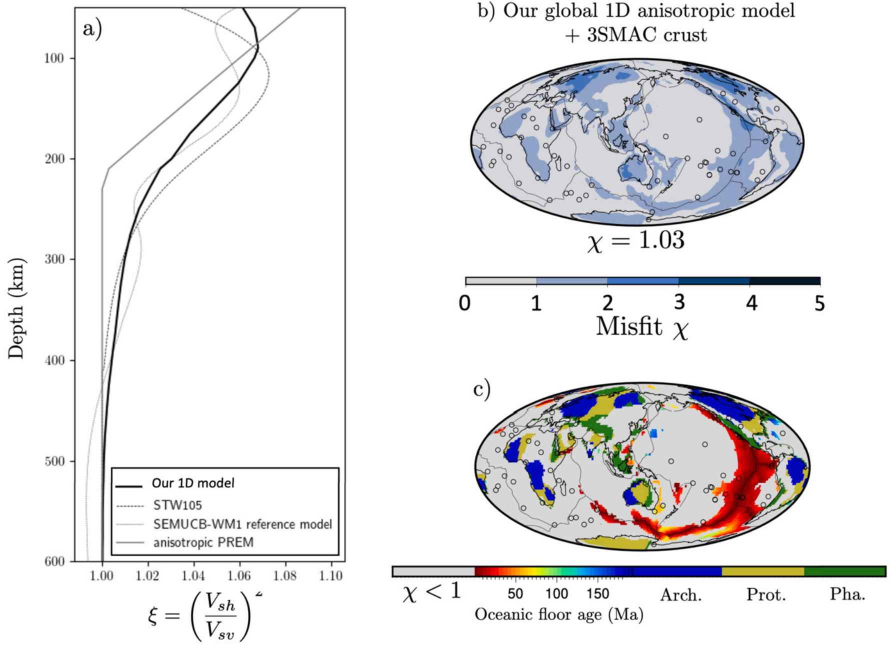

Fig. 2. Existing 1D models and data misfit maps. (a) Various 1D anisotropic models including our global 1D anisotropic model (thick black curve). (b) Maps of the local misfit for our global 1D anisotropic model including a 3SMAC crust on top of it. (c) Same as b) but where $\chi > 1$ regions have been replaced by the nature, continental or oceanic, and age of the terrains.

French and Romanowicz, 2014; Moulik and Ekström, 2014; Chang et al., 2015). The different sets of Rayleigh and Love maps, with their various periods and overtones, are then inverted simultaneously, at each latitude θ and longitude ϕ, to obtain $V_{sv}(\theta,\phi,r)$ and $\xi(\theta,\phi,r)$. The Rayleigh and Love phase velocity maps have been generated with the same regionalization scheme, including the same correlation length. This ensures the lateral coherence of the 1D inversions performed at each geographical point.

Phase velocity perturbations at a period T, $\delta c_T^x(\theta,\phi)$ (x stands for Love or Rayleigh), depend linearly on local variations in V_{sv} and ξ at depth, following:

$$\delta c_T^x(\theta,\phi) = \int_0^a \left[\delta V_{sv}(\theta,\phi,r) K_{V_{sv}}^x(r) + \delta\xi(\theta,\phi,r) K_\xi^x(r)\right] \mathrm{d}r, \tag{1}$$

where a is the Earth radius, $\delta X(\theta,\phi,r)$ are the local parameter variations (θ, ϕ and r, are latitude, longitude and radius) and $K_X^x(r) = \partial c_T^x / \partial X(r)$ the sensitivity kernels for the considered surface wave and period. This formalism implies that we neglect density and P velocity anisotropy variations which are fixed at PREM values. This is reasonable as Rayleigh and Love phase velocities are mainly sensitive to V_{sv} and ξ (Nishimura and Forsyth, 1989).

First, we invert the whole Rayleigh and Love dataset for a global 1-D anisotropic model that is shown Fig. 2a (thick black curve). For this inversion, the *a priori* model, also used to compute the kernels, is the 1-D PREM model (Dziewonski and Anderson, 1981) in which we removed radial anisotropy ($\xi = 1$). The model obtained after inversion is in agreement with other existing 1-D anisotropic models and confirms the presence of a ≈300 km thick, shallow layer of $\xi > 1$. In Fig. 2b, we display the data misfit χ at each location for this 1-D anisotropic model including the local 3SMAC crust on top of it (Nataf and Ricard, 1996). χ is defined as

$$\chi = \sqrt{\frac{1}{N}\sum_{x,T}\left(\frac{c_T^x(\mathrm{obs}) - c_T^x(\mathrm{pred})}{\sigma}\right)^2} \tag{2}$$

where $c_T^x(\mathrm{obs})$ and $c_T^x(\mathrm{pred})$ are the measured and predicted phase velocities and σ are the associated uncertainties. σ is fixed to 0.05 km s^{-1}, which, depending on the mode and period, corresponds to between ≈ 0.6 and 1.2% of the measured Love and Rayleigh phase velocities. This level of uncertainties corresponds to an average error of 5 to 10 s depending on the period of the surface wave mode. It is in agreement with published estimations of uncertainties which includes among other the uncertainties on the source mechanism, location, origin time and the effect of ambient noise (e.g. Moulik et al., 2021). Although the global misfit is close to 1, this χ map reveals that it varies locally. In most places our global 1-D anisotropic model including the local 3SMAC crust is sufficient to explain the data ($\chi < 1$) but locally the data requires a more complex anisotropic structure ($\chi > 1$). In Fig. 2c we have associated the regions of $\chi > 1$ with the nature, continental or oceanic, and age of the terrains. Interestingly, it shows that in most of the oceanic regions and some parts of the youngest continental regions, our global 1-D anisotropic model with the relevant crust is sufficient for explaining the data, while a specific radial anisotropic model is required under cratons and under the young Pacific ocean ridge (below 50 Ma). These conclusions still hold when we use a downgraded Rayleigh dataset with the same ray coverage (≈100 000 rays) as the Love dataset (see Figs. S4a and S4b). This test also shows that a specific radial anisotropic model is required under cratons but it is also required under the Pacific ridge, as well as under some small portions of the Indian and the Atlantic ridges. Cratons are the oldest continental terrains on Earth and the Pacific ridge is the fastest ridge on Earth. These regions are therefore places where current or past deformation have been intense and thus where we can expect a specific radial anisotropic pattern that differs from the global one.

The very poor agreement between all previous 3-D models of radial anisotropy (Fig. 1) most likely indicates that a global and simultaneous inversion of velocity and anisotropy is hampered by trade-offs between 3-D variations of these two quantities, making 3-D radial anisotropy unreliable. To simplify and hopefully make the inversion of anisotropy more robust, we decide to use our observations of Love and Rayleigh phase velocities $\delta c_T^x(\theta,\phi)$ to build a hybrid anisotropic model. In this model we perform an inversion at every geographical point to recover either only the vertical shear velocity, fixing the anisotropy, or both, the

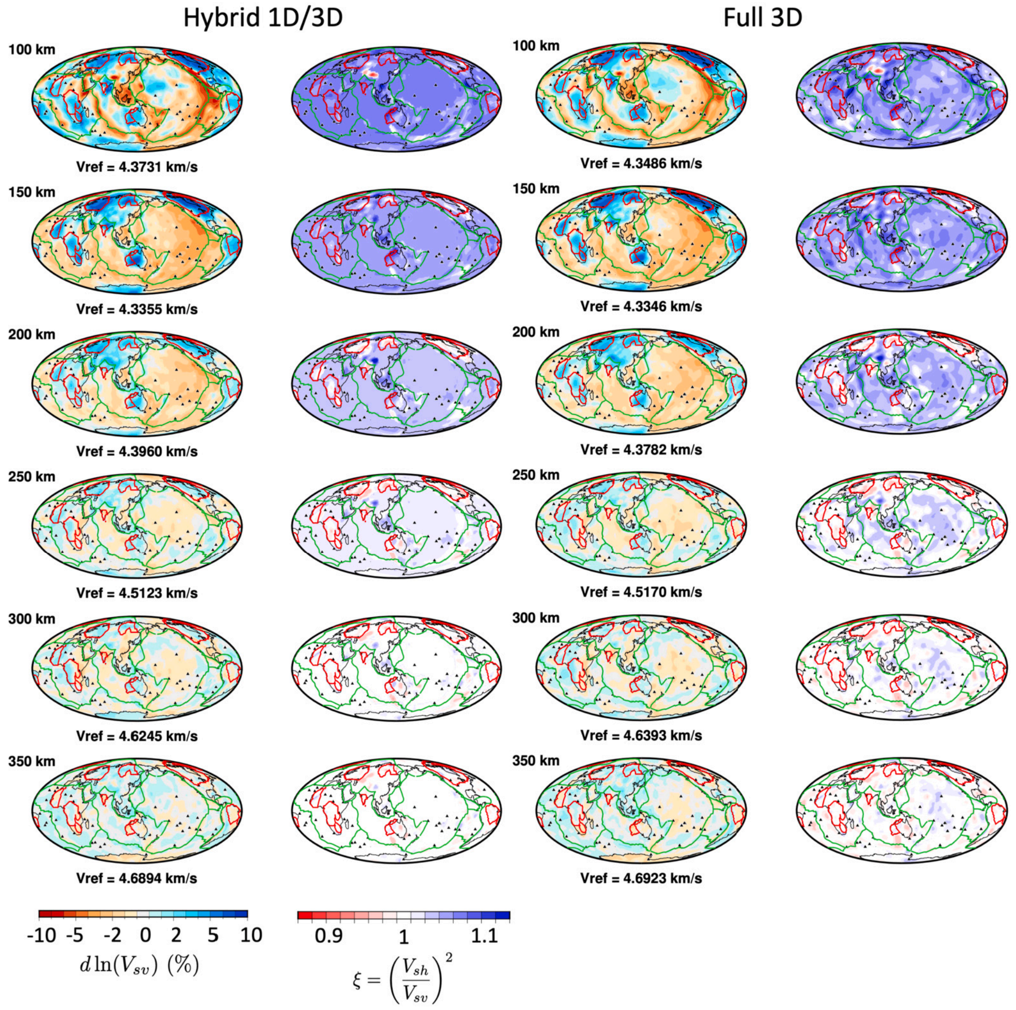

Fig. 3. **V_{sv} and ξ variations for both models, Hybrid 1D/3D and Full 3D**. The V_{sv} model is given in perturbations in % relative to the average velocity at each depth $Vref$ indicated under each plot. The plate boundaries are also indicated in green, the Archean provinces in red and the major hotspots by black triangles.

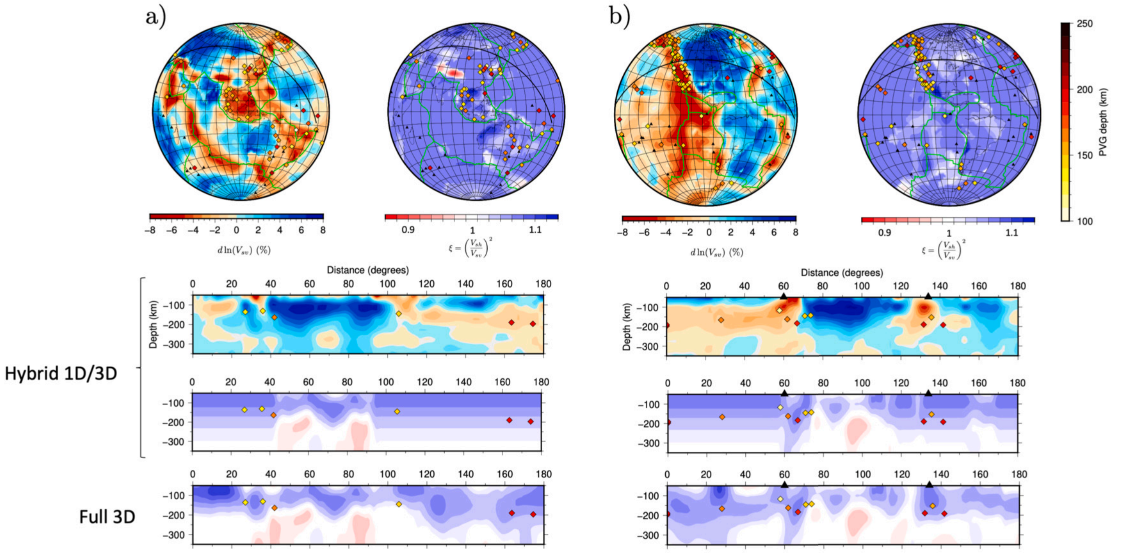

Fig. 4. **Example of cross-sections**. (a) Map view of V_{sv} and ξ variations at 100 km depth. The black line marks the path along which the V_{sv} and ξ cross-sections are shown below. (b) Same as (a) but under Eurasia continent. Hotspots are indicated with black triangles on the maps. The positive velocity gradient (PVG) depths from the global study of Hua et al. (2023) are superimposed on both, the maps and the cross-sections, as colored diamonds according to the colorscale shown on the right of the maps.

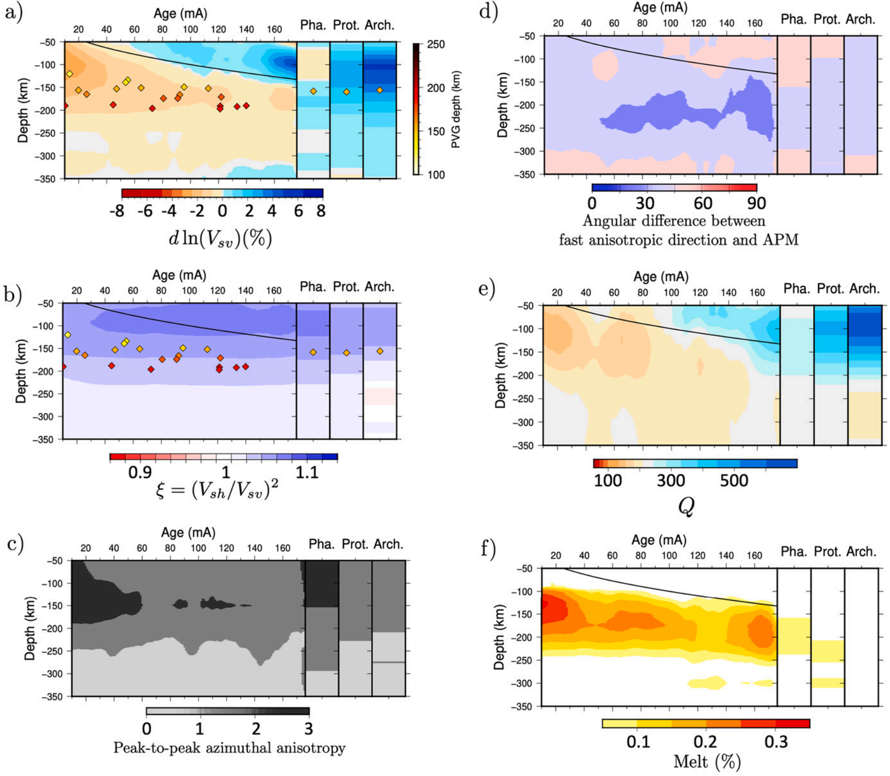

Fig. 5. Oceanic and continental averaged seismic properties. (a) V_{sv} perturbations as a function of age and depth, over oceanic regions and continents where Pha. stands for Phanerozoic, Prot. for Proterozoic, and Arch. for Archean continental provinces. Similar graphs are shown for radial anisotropy ξ (b), peak-to-peak azimuthal anisotropy (c), angular difference between fast anisotropic direction and absolute plate motion (APM), (d), quality factor Q_s (e), melt content (f). On a) and b) are also plotted the averaged positive velocity gradient (PVG) depths from the global study of Hua et al. (2023). For oceanic regions, a continuous image was created by averaging each parameter along the Müller et al. (2008) isochrons, using a sliding window of ± 5 Ma. The continuous black lines indicate the position of the thermal boundary layer for the half-space cooling model (Turcotte and Schubert, 2002). Continental provinces are defined according to 3SMAC (Nataf and Ricard, 1996).

vertical shear velocity and radial anisotropy, according to equation (1). We thus invert for a 1-D V_{sv} model and:

- in regions where our global 1-D anisotropic model including the local 3SMAC crust fits the data ($\chi < 1$ in Fig. 2b), ξ is kept to our global 1-D anisotropic model (Fig. 2a)
- in regions where our global 1-D anisotropic model including the local 3SMAC crust does not fit the data ($\chi > 1$ in Fig. 2b), we invert for the local 1-D ξ model.

We always start from the isotropic PREM model including the local 3SMAC crust. The data covariance matrices for Rayleigh and Love data are always chosen to be diagonal with a constant error of 0.05 km s^{-1}. The parameter covariance matrix C_p is set to a Gaussian correlation function that couples the parameters at different radii with a correlation length $L_c = 50$ km. This controls the vertical smoothness of the model, although velocity and anisotropy are assumed uncorrelated. The amplitude of the covariance for anisotropy decreases with depth and the model is damped towards an isotropic profile as the depth reaches 600 km. We finally obtain the new hybrid upper mantle tomographic model (denoted Hybrid 1D/3D) presented in Fig. 3.

We have also tried to invert for both, local 1D V_{sv} and ξ models, at every geographical point which leads to the model denoted Full 3D shown in Fig. 3. The Full 3D model incorporates 3-D variations everywhere, even in regions where our 1-D anisotropic model including the crust can explain the data (see Fig. 2). These 3-D variations of ξ, not required by the data, are likely due to trade-offs with seismic velocities. This trade-off significantly affects the radial anisotropy $\xi = (V_{sh}/V_{sv})^2$ but is very small for V_{sv}, the hybrid and full 3-D V_{sv} models are visually identical (Fig. 3).

3. The global radially anisotropic model

Fig. 3 displays maps at different depths in our V_{sv} and ξ models for the models Hybrid 1D/3D and Full 3D. The same data are also plotted in Figs. S5 and S6 with a map projection that better highlights the structure beneath cratons. To complement these figures, we show two cross-sections in Fig. 4, as well as oceanic and continental averages for Phanerozoic, Proterozoic, and Archean continental provinces in Fig. 5a-b.

Our V_{sv} model confirms that global velocity perturbations are in agreement with previous tomographic models (Fig. 1). It shows a strong correlation with surface tectonics in the uppermost 300 km (Fig. 3). Down to a depth of 150 km, slow velocities are observed beneath mid-oceanic ridges and V_{sv} increases in oceanic regions with sea-floor age. Back-arc, active tectonic and Phanerozoic regions are generally slow while Precambrian continents display fast velocities. A clear difference is observed at depths ranging from 150 to 250 km, between continents and younger Phanerozoic and oceanic regions, displaying fast and slow seismic velocities, respectively. The cross-sections in Fig. 4 and the age-average velocity in Fig. 5a show the well-known thickening of the seismically fast oceanic lithosphere with age (e.g. Maggi et al., 2006). Differences in lithospheric thicknesses between continents and oceans are also clearly visible: the high velocity lid associated with the lithosphere has a thickness of about 125 km for the oldest oceanic ages, while it can reach up to 300 km beneath Proterozoic and Archean continental lithospheres (Fig. 4).

The 3-D ξ variations are quite different. On average, the radial anisotropy ξ is greater than one down to 250 km depth. This feature is consistent with all the models that have attempted to measure ξ, including PREM: near the surface, the horizontally polarized S waves propa-

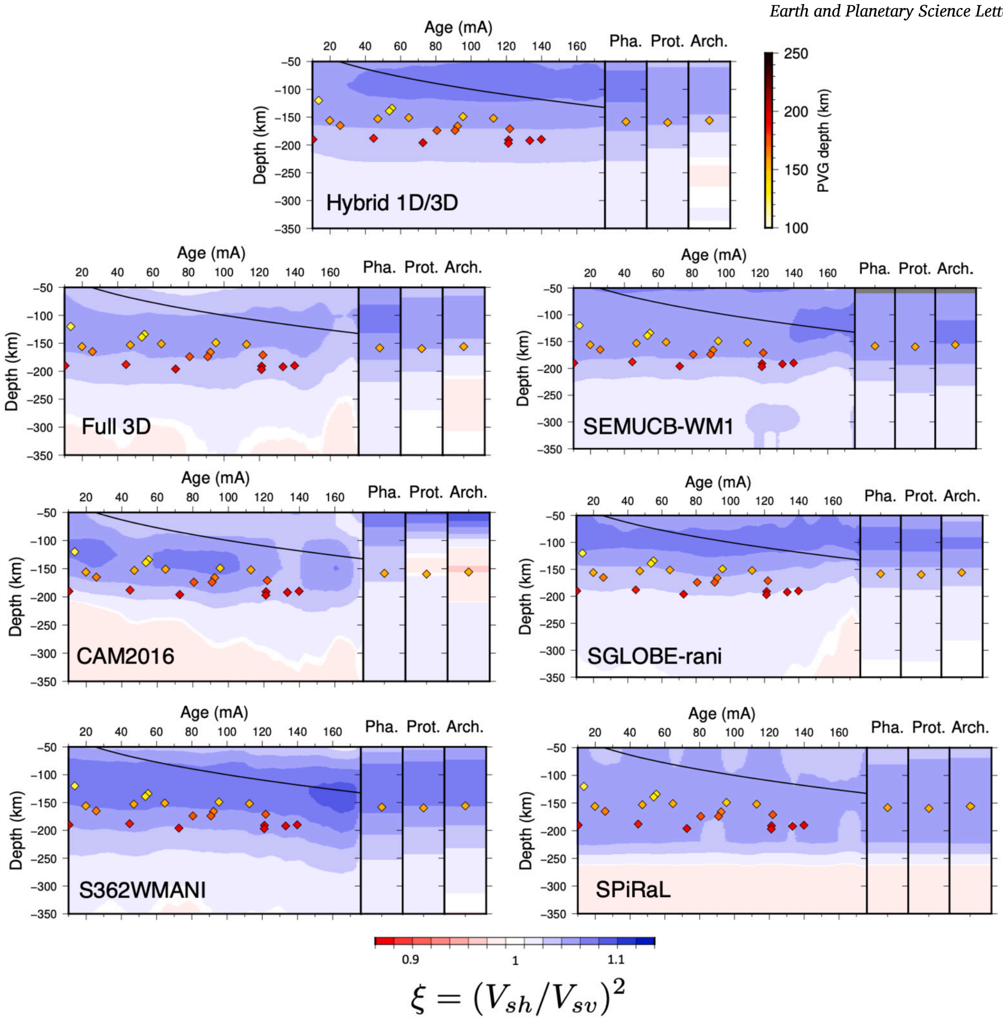

Fig. 6. Comparison of oceanic and continental averaged ξ for different radially anisotropic models. CAM2016: Priestley et al. (2020), S362WMANI: Kustowski et al. (2008), SEMUCB-WM1: French and Romanowicz (2014), SGLOBE-rani: Chang et al. (2015), SPiRaL: Simmons et al. (2021).

gate faster than the vertically polarized S waves (see Fig. 1). Deeper, there are more regions where ξ is less than 1 that do not show obvious correlations with surface tectonic structures. By construction, the value of ξ under oceans is mostly independent of the lithospheric age since ξ has been fixed to our 1-D anisotropic model in most of the oceans (Fig. 5b). However, even the Full 3-D inversion confirms this feature for ages greater than 40 Myrs (Fig. 6). The oceanic ξ variations are thus characterized by a constant 300 km thick layer where $\xi \geq 1$. This age-independent ξ is also observed in other radially anisotropic tomographic models (see also Burgos et al., 2014; Beghein et al., 2014), only CAM2016 and our Full 3-D model suggest a vague age dependence of ξ at ages smaller than 40 Myrs (Fig. 6). Under continents, our results favor a two layer structure for the Archean lithosphere, with $\xi > 1$ in an upper layer down to ~225 km depth, and ξ slightly less than 1, in the underlying 50 km thick layer (Figs. 3, 4 and 5). This agrees with regional models produced under North America (see e.g. Hua et al., 2025) and Asia (see e.g. Ma et al., 2023). Ma et al. (2023) report a peak of ξ at around 120 km depth and $\xi < 1$ beneath, from 230 to 300 km depth. This is in particularly good agreement with our model as shown on Fig. 4a. The $\xi < 1$ region beneath the craton is interpreted as the imprint of a hot plume or of surrounding slabs. Hua et al. (2025) make similar observations under the North American craton, which also agree with our model (Fig. 4b). In their study, they describe drip-like features at the base of the craton that correspond well with our $\xi < 1$ anomaly. It is interpreted as an active lithospheric thinning induced by the sinking of the Farallon plate. On a global scale, Priestley et al. (2020) also observed a $\xi < 1$ layer beneath cratons, but located shallower within the continental lithosphere (from 100 km down to 200 km), and thicker than ours (Fig. 6). Priestley et al. (2020) interpret their observation as the record of a significant compression stage resulting in a thickening of the lithosphere by a factor of about two. This $\xi < 1$ anisotropy could also be the result of past delamination processes (e.g. Hu et al., 2018) due to the thermal erosion of the cratons (e.g. Foley, 2008; Celli et al., 2020). A $\xi < 1$ layer is also observed in SPiRaL, but this is not specific to Archean terrains, it is visible everywhere in the oceanic and continent parts from 250 km depth. A $\xi < 1$ layer is not found in other models (Fig. 6), although they all suggest a weaker ξ in the asthenosphere. The $\xi < 1$ layer observed in our model suggests a more pronounced reduction at the base of the Archean lithosphere than previously observed. In SPIRaL and SEMUCB-WM1, no tectonic dependence of anisotropy is observed globally, not even between continents and oceans. All these models of craton anisotropy contrast with Gung et al. (2003) and Yuan and Romanowicz (2010), who suggested that cratons are characterized by a weak anisotropic lithosphere underlaid by a $\xi > 1$ asthenospheric mantle.

In Figs. S4c and S4d we provide some depths slices as well as the oceanic and continental averages for the Hybrid 1D/3D ξ model obtained with the downgraded Rayleigh dataset. They show a similar anisotropic pattern: ξ is age independent under the oceanic regions and exhibits two layers under the craton. The main difference concerns the $\xi < 1$ anomaly under cratons which, instead of being restricted to a 50 km thick layer, extends deeper into the mantle down to a depth of at least 350 km. In summary, our results are not significantly affected by the difference of ray coverage between the Rayleigh and Love datasets, and the same conclusions apply.

Note that the misfit after inversion of the Full 3D model is no better than that of the Hybrid 1D/3D model. The chi-square value is $\chi = 0.22$ for both, which is ≈ 5 times smaller than the misfit before inversion (see Fig. S7). This confirms that the lateral variations of the anisotropic signal are only necessary beneath cratons and young oceans. In the other regions, the signal obtained by the Full 3D inversion has no impact on the misfit. This signal belongs to the null-space of the forward operator (de Wit et al., 2012). The trade-off between velocities and anisotropy is very small for V_{sv} (Fig. 3) but affects significantly the ratio $\xi = (V_{sh}/V_{sv})^2$. The Full 3D model merely illustrates the spurious signal that arises from overfitting the data. Our preferred model is the more parsimonious Hybrid 1D/3D.

To summarize, V_{sv} and ξ variations display opposite trends that are well illustrated in Fig. 4 on specific cross-sections. For V_{sv}, a clear age-dependent transition between lithosphere and asthenosphere is observed under oceans, which is less clear under continents and cratons, where strong and fast anomalies are present down to 200-250 km deep. On the contrary, for ξ, the age-dependent lithosphere - asthenosphere transition is absent under oceans and we observe an almost uniform 250 km thick layer with $\xi > 1$. Beneath continental and cratonic regions, two layers of anisotropy are found, with $\xi > 1$ down to 225 km depth in a top layer and $\xi < 1$ in a 50 km thick lower layer. This transition from $\xi > 1$ to $\xi < 1$ from 150 to 225 km seems to coincide with a positive velocity gradient (PVG) recently detected in a global receiver function study (Hua et al., 2023). Using the same dataset but a Bayesian approach for the depth inversion, Boyce et al. (2024) also detect this mid-lithospheric low velocity layer whose lower interface could correspond to the PVG. Although such thin structures can hardly be seen using long-wavelength data, they may separate thicker layers with a different seismic signature which we image here. Finally, as in other studies, we do not observe the imprints of the plumes or the slabs in the ξ variations. This is due to the fact that slabs and plumes belong to regions where a 1-D average model is sufficient. This may also be due to the resolution limit imposed by the use of long period surface waves.

ξ variations can also be compared with our previous azimuthal anisotropy model (Debayle and Ricard, 2012). In this paper, Debayle and Ricard (2012) discuss the relationship between the direction of azimuthal anisotropy and the plate motions. They distinguish between the absolute plate motion, APM, and the fossil accretion velocity, FAV (i.e. the gradient of the plate age). They suggest that the shallow azimuthal anisotropy is frozen in the lithosphere, as better correlated with FAV than with APM, although the difference between APM and FAV is small and restricted to a limited domain of the old oceanic floor. Fig. 5c shows the averaged azimuthal anisotropy strength and Fig. 5d the angular difference between the fast azimuthal anisotropy direction and the absolute plate motion (APM). Azimuthal anisotropy is at first order independent of lithospheric age (Fig. 5c-d). However, it varies with plate velocities and the azimuthally anisotropic layer extends slightly deeper under fast moving plates (Fig. 7a). A similar observation can be done for ξ (Fig. 7b): the radial anisotropy under the fast spreading pacific ridge extends deeper than under the other slower ridges. Since azimuthal anisotropy indicates a preferred orientation of crystals in the horizontal direction, a strong azimuthal anisotropy is expected to coincide with $\xi > 1$.

Figs. 5e and 5f complete our age-averaged cross sections with Q_s and a melt content section. The Q_s is an average cross section in QsADR17, our recent quality factor model (Adenis et al., 2017) while the melt content section was obtained from the simultaneous interpretation of our V_{sv} and Q_s models (Debayle et al., 2020) by comparing velocity and attenuation to laboratory observations (Takei, 2017). Oceanic regions are characterized by high attenuation and a small melt proportion in the asthenosphere, which roughly follows the thermal thickening of the oceanic lithosphere. The cratonic lithosphere appears weakly attenuating and melt free.

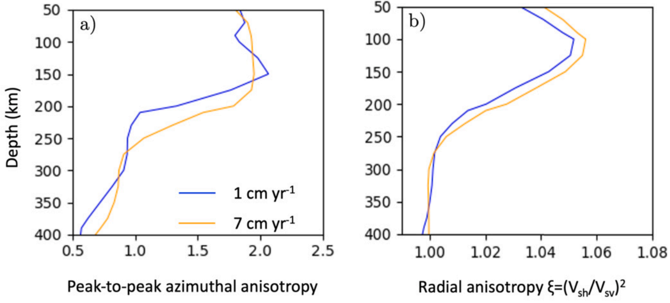

Fig. 7. Averaged azimuthal and radial anisotropy depth profiles for slow and fast plates. The depth variations of peak-to-peak azimuthal anisotropy (a) and radial anisotropy (b) are displayed for slow (1 cm yr^{-1}) and fast (7 cm yr^{-1}). The properties have been averaged for all geographical points with similar plate velocities (± 2 cm yr^{-1}).

4. A lithosphere - asthenosphere system conceptual model

In this section, we propose a conceptual model of the lithosphere - asthenosphere system (Fig. 8). This model is based on our V_{sv}, ξ, azimuthal anisotropy, Q_s and melt content observations. It summarizes all our seismic findings.

The conceptual model of Fig. 8 emphasizes the major structural differences between oceanic and continental lithospheres. Under the oceans, the velocities are mainly a function of the age of the seafloor. The lithosphere is thin, reaching no more than ≈ 125 km at the oldest ages. Beneath the lithosphere, the mantle appears homogeneous and adiabatic, with no dynamic upwelling beneath ridges excepted may be beneath the East Pacific-Rise where a weaker ξ might suggest vertical flow. Azimuthal anisotropy is mainly confined around a depth of 150 km, but also shows some dependence with the seafloor age. In the asthenosphere, the directions of fast propagation are largely controlled by the actual plate motion, particularly under fast-moving plates. In the oceanic lithosphere, the direction of fast propagation is probably frozen, with a slightly better angular correlation with the age gradient than with the APM (the two directions are only identical if the orientation of the Euler rotation axis of the plate has never changed). Attenuation is more difficult to quantify, but seems also age dependent. Comparison with laboratory data indicates that attenuation cannot be explained by temperature only and suggests the presence of a small quantity of partial melt trapped in the asthenosphere (maximum 0.3%). The radial anisotropy shows no correlation with age, and appears mostly localized at a constant depth range, $\approx 100 - 200$ km. Consistent with the horizontal shear indicated by the azimuthal anisotropy, ξ is greater than 1 and horizontally polarized S-waves are faster than vertically polarized S-waves. It is only below the ultra-fast Pacific-Nazca Ridge that some reduction in radial anisotropy underlines the presence of vertical flow in the mantle.

This model is in overall agreement with Auer et al. (2015), although we propose that small melt fractions are present everywhere in the asthenospheric mantle under oceans, not only beneath hotspots (Auer et al., 2015; Schmerr, 2012). This molten material is likely trapped along the interfaces of mineralogical grains contributing to the observation of a radial $\xi > 1$ and azimuthal anisotropy little dependent on the age of the ocean floor. In the asthenosphere, oriented melt pockets and flow induced orientation of olivine crystals (CPO - Crystallographic Preferred Orientation) would further contribute to the observed $\xi > 1$. The flow induced CPO also explains the observed alignment of azimuthal anisotropy with APM observed under fast moving plates (Debayle and Ricard, 2012).

Beneath old continental regions, the transition from lithosphere to asthenosphere occurs deeper and is less conspicuous. We observe a seis-

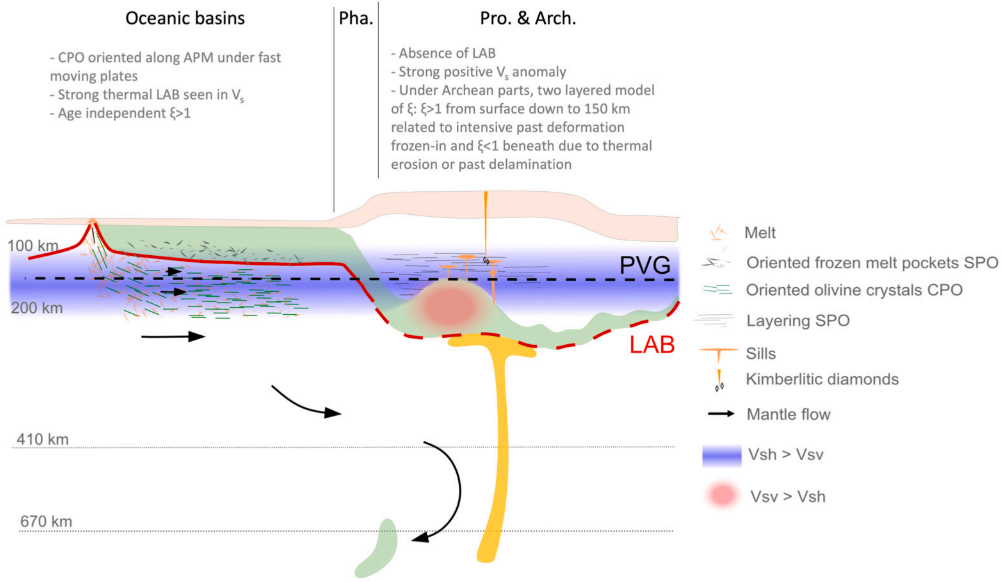

Fig. 8. Schematic cartoon of the lithosphere - asthenosphere system.

mically fast and thick lithosphere. The ξ structure, on the contrary, highlights a top lithospheric layer, strongly anisotropic and characterized by $\xi > 1$. This anisotropic layer can be explained by the intense layering recorded during past deformations as well as by sills testifying past metasomatism and underlying the layering (see e.g. Griffin et al., 1999). Beneath this layer, the weaker or negative ($\xi < 1$) anisotropic layer could correspond to the thermal lithosphere where past delaminations (see e.g. Hu et al., 2018) would have occurred and thus where some vertical flow is either on-going or has been recorded.

5. Concluding remarks

An important result of this study is the observation that a 1-D radially anisotropic model including a proper crust fits surface waves data in most regions of the Earth. It is only beneath cratons and fast spreading ridges for ages under 40 Ma, that lateral variations of radial anisotropy are required. We believe that the large discrepancies between previous models of radial anisotropy are primarily due to the overfitting of data in regions where lateral variations in radial anisotropic are not necessary. The upwelling flow decreases ξ below 1 beneath the fastest ridges and vertical motion is also witnessed below the cratonic lithosphere.

We propose that the thicker radially anisotropic layer under the oceans compared to the continents indicates a change in origin from an anisotropy frozen under the continent to a more complex situation under the oceans. Under the continents, a chemically depleted top layer with high anisotropy ($\xi > 1$), reflecting intense layering during past deformation, would overlain a weaker anisotropic layer ($\xi < 1$), probably reflecting past compression. Under the oceans, molten material is probably trapped along mineralogical grain interfaces in the deep lithosphere. This melt may have been acquired at mid-ocean ridges. In the oceanic asthenosphere, oriented melt pockets and flow-induced crystallographic orientation of olivine crystals would explain the radial anisotropy, the alignment of the azimuthal anisotropy with the APM under fast-moving plates, and the presence of small fractions of melt throughout the asthenosphere. In the shallow layers, azimuthal anisotropy may be frozen and aligned with the rate of fossil accretion rather than APM.

Our understanding of the lithosphere-asthenosphere system has been improved considerably thanks to the ability of seismic studies to map independent parameters such as V_s, azimuthal and radial anisotropy ξ and attenuation Q. Each of these observations testifies to different physical effects related to temperature, composition or flow giving an overview of the Earth's shallow layers. However, the quality of the different observations that seismology can provide is still uneven, with good agreement between all tomographic models of velocity and azimuthal anisotropy, and still significant uncertainty in attenuation and radial anisotropy. It is certainly in these domains that future effort should be concentrated.

CRediT authorship contribution statement

S. Durand: Writing – review & editing, Writing – original draft, Methodology, Data curation, Conceptualization. **E. Debayle:** Writing – review & editing, Writing – original draft, Methodology, Data curation, Conceptualization. **Y. Ricard:** Writing – review & editing, Writing – original draft, Methodology, Conceptualization.

Declaration of competing interest

The authors declare that they have no known competing financial interests or personal relationships that could have appeared to influence the work reported in this paper.

Acknowledgements

S.D., E.D. and Y.R. are supported by the French ANR project JIGSAW2 ANR-20-CE49-0001-01. We thank the two anonymous reviewers for their helpful comments that improved the manuscript.

Appendix A. Supplementary material

Supplementary material related to this article can be found online at https://doi.org/10.1016/j.epsl.2025.119720.

Data availability

The data and models are available on S. Durand website (https://perso.ens-lyon.fr/stephanie.durand).

References

Adenis, A., Debayle, E., Ricard, Y., 2017. Attenuation tomography of the upper mantle. Geophys. Res. Lett. 44, 7715–7724. https://doi.org/10.1002/2017GL073751.

Audhkhasi, P., Singh, S.C., 2022. Discovery of distinct lithosphere-asthenosphere boundary and the Gutenberg discontinuity in the Atlantic Ocean. Sci. Adv. 8, eabn5404.

Auer, L., Becker, T.W., Boschi, L., Schmerr, N., 2015. Thermal structure, radial anisotropy, and dynamics of Oceanic boundary layers. Geophys. Res. Lett. 42, 9740–9749.

Becker, T.W., 2008. Azimuthal seismic anisotropy constrains net rotation of the lithosphere. Geophys. Res. Lett. 35. https://doi.org/10.1029/2007GL032928. https://agupubs.onlinelibrary.wiley.com/doi/abs/10.1029/2007GL032928. https://agupubs.onlinelibrary.wiley.com/doi/pdf/10.1029/2007GL032928.

Becker, T.W., Lebedev, S., 2021. Dynamics of the Upper Mantle in Light of Seismic Anisotropy. American Geophysical Union (AGU), pp. 257–282. Chapter 10. https://agupubs.onlinelibrary.wiley.com/doi/abs/10.1002/9781119528609.ch10. https://agupubs.onlinelibrary.wiley.com/doi/pdf/10.1002/9781119528609.ch10.

Beghein, C., Yuan, K., Schmerr, N., Xing, Z., 2014. Changes in seismic anisotropy shed light on the nature of the Gutenberg discontinuity. Science 343, 1237–1240. https://doi.org/10.1126/science.1246724.

Billien, M., Lévêque, J.J., Trampert, J., 2000. Global maps of Rayleigh wave attenuation for periods between 40 and 150 seconds. Geophys. Res. Lett. 27, 3619–3622.

Boyce, A., Bodin, T., Durand, S., Soergel, D., Debayle, E., 2024. Seismic evidence for craton formation by underplating and development of the mld. Geophys. Res. Lett. 51, e2023GL106170. https://doi.org/10.1029/2023GL106170.

Burgos, G., Montagner, J.P., Beucler, E., Capdeville, Y., Mocquet, A., Drilleau, M., 2014. Oceanic lithosphere-asthenosphere boundary from surface wave dispersion data. J. Geophys. Res. 119, 1079–1093. https://doi.org/10.1002/2013JB010528.

Celli, N.L., Lebedev, S., Schaeffer, A.J., Gaina, C., 2020. African cratonic lithosphere carved by mantle plumes. Nat. Commun. 11, 92. https://doi.org/10.1038/s41467-019-13871-2.

Chang, S.J., Ferreira, A.M., Ritsema, J., van Heijst, H.J., Woodhouse, J.H., 2014. Global radially anisotropic mantle structure from multiple datasets: a review, current challenges, and outlook. Tectonophysics 617, 1–19. https://doi.org/10.1016/j.tecto.2014.01.033. https://www.sciencedirect.com/science/article/pii/S0040195114000699.

Chang, S.J., Ferreira, A.M.G., Ritsema, J., van Heijst, H.J., Woodhouse, J.H., 2015. Joint inversion for global isotropic and radially anisotropic mantle structure including crustal thickness perturbations. J. Geophys. Res. 120, 4278–4300. https://doi.org/10.1002/2014JB011824.

Dalton, C.A., Ekstroem, G., Dziewonski, A.M., 2008. The global attenuation structure of the upper mantle. J. Geophys. Res. 113. https://doi.org/10.1029/2007JB005429.

Debayle, E., Bodin, T., Durand, S., Ricard, Y., 2020. Seismic evidence for partial melt below tectonic plates. Nature 586, 555–559. https://doi.org/10.1038/s41586-020-2809-4.

Debayle, E., Dubuffet, F., Durand, S., 2016. An automatically updated s-wave model of the upper mantle and the depth extent of azimuthal anisotropy. Geophys. Res. Lett. 43, 674–682. https://doi.org/10.1002/2015GL067329.

Debayle, E., Kennett, B., 2000. Anisotropy in the Australasian upper mantle from Love and Rayleigh waveform inversion. Earth Planet. Sci. Lett. 184, 339–351.

Debayle, E., Ricard, Y., 2012. A global shear velocity model of the upper mantle from fundamental and higher Rayleigh mode measurements. J. Geophys. Res., Solid Earth 117.

Debayle, E., Ricard, Y., 2013. Seismic observations of large-scale deformation at the bottom of fast-moving plates. Earth Planet. Sci. Lett. 376, 165–177.

Debayle, E., Sambridge, M., 2004. Inversion of massive surface wave data sets: model construction and resolution assessment. J. Geophys. Res. 109. https://doi.org/10.1029/2003JB002652.

Durand, S., Debayle, E., Ricard, Y., 2015. Rayleigh wave phase velocity and error maps up to the fifth overtone. Geophys. Res. Lett. 42, 3266–3272. https://doi.org/10.1002/2015GL063700.

Dziewonski, A.M., Anderson, D.L., 1981. Preliminary reference Earth model. Phys. Earth Planet. Inter. 25, 297–356.

Ferreira, A.M.G., Woodhouse, J.H., Visser, K., Trampert, J., 2010. On the robustness of global radially anisotropic surface wave tomography. J. Geophys. Res., Solid Earth 115. https://doi.org/10.1029/2009JB006716. https://agupubs.onlinelibrary.wiley.com/doi/abs/10.1029/2009JB006716. https://agupubs.onlinelibrary.wiley.com/doi/pdf/10.1029/2009JB006716.

Foley, S.F., 2008. Rejuvenation and erosion of the cratonic lithosphere. Nat. Geosci. 1, 503–510. https://doi.org/10.1038/ngeo261.

French, S.W., Romanowicz, B.A., 2014. Whole-mantle radially anisotropic shear velocity structure from spectral-element waveform tomography. Geophys. J. Int. 199, 1303–1327. https://doi.org/10.1093/gji/ggu334.

Griffin, W.L., Doyle, B.J., Ryan, C.G., Pearson, N.J., Suzanne, Y.O., Davies, R., Kivi, K., Van Achterbergh, E., Natapov, L.M., 1999. Layered mantle lithosphere in the Lac de Gras area, Slave Craton: composition, structure and origin. J. Petrol. 40, 705–727. https://doi.org/10.1093/petroj/40.5.705.

Gung, Y., Panning, M., Romanowicz, B., 2003. Global anisotropy and the thickness of continents. Nature 422, 707–711.

Gung, Y., Romanowicz, B., 2004. Q tomography of the upper mantle using three-component long-period waveforms. Geophys. J. Int. 157, 813–830. https://doi.org/10.1111/j.1365-246X.2004.02265.x.

Ho, T., Priestley, K., Debayle, E., 2016. A global horizontal shear velocity model of the upper mantle from multimode Love wave measurements. Geophys. J. Int. 207, 542–561. https://doi.org/10.1093/gji/ggw292.

Hu, J., Liu, L., Faccenda, M., Zhou, Q., Fischer, K.M., Marshak, S., Lundstrom, C., 2018. Modification of the western Gondwana craton by plume–lithosphereinteraction. Nat. Geosci. 11, 203–210. https://doi.org/10.1038/s41561-018-0064-1.

Hua, J., Fischer, K.M., Becker, T.W., Gazel, E., Hirth, G., 2023. Asthenospheric low-velocity zone consistent with globally prevalent partial melting. Nat. Geosci. 16, 175–181.

Hua, J., Grand, S.P., Becker, T.W., Janiszewski, H.A., Liu, C., Trugman, D.T., Zhu, H., 2025. Seismic full-waveform tomography of active cratonic thinning beneath North America consistent with slab-induced dripping. Nat. Geosci. 18, 358–364.

Karaoğlu, H., Romanowicz, B., 2018. Inferring global upper-mantle shear attenuation structure by waveform tomography using the spectral element method. Geophys. J. Int. 213, 1536–1558. https://doi.org/10.1093/gji/ggy030. https://academic.oup.com/gji/article-pdf/213/3/1536/24455634/ggy030.pdf.

Kustowski, B., Ekström, G., Dziewoński, A.M., 2008. Anisotropic shear-wave velocity structure of the Earth's mantle: a global model. J. Geophys. Res. 113. https://doi.org/10.1029/2007JB005169.

Lebedev, S., Van Der Hilst, R.D., 2008. Global upper-mantle tomography with the automated multimode inversion of surface and s-wave forms. Geophys. J. Int. 173, 505–518. https://doi.org/10.1111/j.1365-246X.2008.03721.x. https://academic.oup.com/gji/article-pdf/173/2/505/6078939/173-2-505.pdf.

Long, M.D., Becker, T.W., 2010. Mantle dynamics and seismic anisotropy. Earth Planet. Sci. Lett. 297, 341–354. https://doi.org/10.1016/j.epsl.2010.06.036. https://www.sciencedirect.com/science/article/pii/S0012821X10004115.

Ma, J., Bunge, H.P., Fichtner, A., Chang, S.J., Tian, Y., 2023. Structure and dynamics of lithosphere and asthenosphere in Asia: a seismological perspective. Geophys. Res. Lett. 50, e2022GL101704.

Ma, Z., Masters, G., Mancinelli, N., 2015. Two-dimensional global Rayleigh wave attenuation model by accounting for finite-frequency focusing and defocusing effect. Geophys. J. Int. 204, 631–649.

Maggi, A., Debayle, E., Priestley, K., Barruol, G., 2006. Multimode surface waveform tomography of the Pacific Ocean: a closer look at the lithospheric cooling signature. Geophys. J. Int. 166, 1384–1397. https://doi.org/10.1111/j.1365-246X.2006.03037.x.

Montagner, J.P., 1994. Can seismology tell us anything about convection in the mantle? Rev. Geophys. 32, 115–137. https://doi.org/10.1029/94RG00099. https://agupubs.onlinelibrary.wiley.com/doi/abs/10.1029/94RG00099.

Montagner, J.P., Tanimoto, T., 1991. Global upper mantle tomography of seismic velocities and anisotropies. J. Geophys. Res. 96, 20337–20351. https://doi.org/10.1029/91JB01890.

Moulik, P., Ekström, G., 2014. An anisotropic shear velocity model of the Earth's mantle using normal modes, body waves, surface waves and long-period waveforms. Geophys. J. Int. 199, 1713–1738.

Moulik, P., Lekic, V., Romanowicz, B., Ma, Z., Schaeffer, A., Ho, T., Beucler, E., Debayle, E., Deuss, A., Durand, S., Ekström, G., Lebedev, S., Masters, G., Priestley, K., Ritsema, J., Sigloch, K., Trampert, J., Dziewonski, A.M., 2021. Global reference seismological data sets: multimode surface wave dispersion. Geophys. J. Int. 228, 1808–1849. https://doi.org/10.1093/gji/ggab418.

Müller, R.D., Sdrolias, M., Gaina, C., Roest, W.R., 2008. Age, spreading rates, and spreading asymmetry of the world's ocean crust. Geochem. Geophys. Geosyst. 9. https://doi.org/10.1029/2007GC001743, 2008.

Nataf, H., Nakanishi, I., Anderson, D., 1986. Measurements of mantle wave velocities and inversion for lateral heterogeneities and anisotropy 3. Inversion. J. Geophys. Res. 91, 7261–7307. https://doi.org/10.1029/JB091iB07p07261.

Nataf, H.C., Ricard, Y., 1996. 3smac: an a priori tomographic model of the upper mantle based on geophysical modeling. Phys. Earth Planet. Inter. 95, 101–122. https://doi.org/10.1016/0031-9201(95)03105-7.

Nishimura, C., Forsyth, D.W., 1989. The anisotropic structure of the upper mantle in the Pacific. Geophys. J. Int. 96, 203–229.

Priestley, K., Ho, T., McKenzie, D., 2020. The formation of continental roots. Geology 49, 190–194. https://doi.org/10.1130/G47696.1.

Priestley, K., McKenzie, D., 2013. The relationship between shear wave velocity, temperature, attenuation and viscosity in the shallow part of the mantle. Earth Planet. Sci. Lett. 381, 78–91.

Ritsema, J., van Heijst, H., Woodhouse, J., 2004. Global transition zone tomography. J. Geophys. Res. 109, B02302. https://doi.org/10.1029/2003JB002610.

Rychert, C.A., Shearer, P.M., Fischer, K.M., 2010. Scattered wave imaging of the lithosphere–asthenosphere boundary. Lithos 120, 173–185.

Savage, M.K., 1999. Seismic anisotropy and mantle deformation: what have we learned from shear wave splitting? Rev. Geophys. 37, 65–106. https://doi.org/10.1029/98RG02075. https://agupubs.onlinelibrary.wiley.com/doi/abs/10.1029/98RG02075.

Schaeffer, A.J., Lebedev, S., 2013. Global shear speed structure of the upper mantle and transition zone. Geophys. J. Int. 194, 417–449. https://doi.org/10.1093/gji/ggt095. https://academic.oup.com/gji/article-pdf/194/1/417/5898775/ggt095.pdf.

Schmerr, N., 2012. The Gutenberg discontinuity: melt at the lithosphere-asthenosphere boundary. Science 335, 1480–1483. https://doi.org/10.1126/science.1215433.

Selby, N., Woodhouse, J., 2002. The *Q* structure of the upper mantle: constraints from Rayleigh wave amplitudes. J. Geophys. Res. 107, 2097. https://doi.org/10.1029/2001JB000257.

Silver, P.G., Chan, W.W., 1991. Shear wave splitting and subcontinental mantle deformation. J. Geophys. Res., Solid Earth 96, 16429–16454. https://doi.org/10.1029/91JB00899. https://agupubs.onlinelibrary.wiley.com/doi/abs/10.1029/91JB00899.

Simmons, N.A., Myers, S.C., Morency, C., Chiang, A., Knapp, D.R., 2021. SPiRaL: a multiresolution global tomography model of seismic wave speeds and radial anisotropy variations in the crust and mantle. Geophys. J. Int. 227, 1366–1391. https://doi.org/10.1093/gji/ggab277.

Takei, Y., 2017. Effects of partial melting on seismic velocity and attenuation: a new insight from experiments. Annu. Rev. Earth Planet. Sci. 45, 447–470. https://doi.org/10.1146/annurev-earth-063016-015820.

Takeuchi, H., Saito, M., 1972. Seismic surface waves. In: Bolt, B.A. (Ed.), Seismology: Surface Waves and Earth Oscillations. Elsevier. In: Methods in Computational Physics: Advances in Research and Applications, vol. 11, pp. 217–295. https://www.sciencedirect.com/science/article/pii/B9780124608115500106.

Tanimoto, T., Anderson, D.L., 1984. Mapping convection in the mantle. Geophys. Res. Lett. 11, 287–290. https://doi.org/10.1029/GL011i004p00287. https://agupubs.onlinelibrary.wiley.com/doi/abs/10.1029/GL011i004p00287.

Tarantola, A., Valette, B., 1982. Generalized nonlinear inverse problems solved using the least squares criterion. Rev. Geophys. 20, 219–232. https://doi.org/10.1029/RG020i002p00219.

Trampert, J., Woodhouse, J.H., 1995. Global phase velocity maps of Love and Rayleigh waves between 40 and 150 seconds. Geophys. J. Int. 122, 675–690. https://doi.org/10.1111/j.1365-246X.1995.tb07019.x. https://onlinelibrary.wiley.com/doi/abs/10.1111/j.1365-246X.1995.tb07019.x. https://onlinelibrary.wiley.com/doi/pdf/10.1111/j.1365-246X.1995.tb07019.x.

Turcotte, D.L., Schubert, G., 2002. Geodynamics. Cambridge University Press.

de Wit, R.W.L., Trampert, J., van der Hilst, R.D., 2012. Toward quantifying uncertainty in travel time tomography using the null-space shuttle. J. Geophys. Res., Solid Earth 117. https://doi.org/10.1029/2011JB008754. https://agupubs.onlinelibrary.wiley.com/doi/abs/10.1029/2011JB008754.

Woodhouse, J.H., Wong, Y.K., 1986. Amplitude, phase and path anomalies of mantle waves. Geophys. J. Int. 87, 753–773. http://gji.oxfordjournals.org/content/87/3/753.short.

Zhang, Yu-Shen, Tanimoto, T., 1991. Global love wave phase velocity variation and its significance to plate tectonics. Phys. Earth Planet. Inter. 66, 160–202.

Yuan, H., Romanowicz, B., 2010. Lithospheric layering in the North American craton. Nature 466, 1063–1068.

Zhou, Y., Nolet, G., Dahlen, F.A., Laske, G., 2006. Global upper-mantle structure from finite-frequency surface-wave tomography. J. Geophys. Res., Solid Earth 111. https://doi.org/10.1029/2005JB003677.